Ocean Dynamics (2018) 68:391–410
https://doi.org/10.1007/s10236-018-1136-x

Submesoscale features and their interaction with fronts and internal tides in a high-resolution coupled atmosphere-ocean-wave model of the Bay of Bengal

Tommy G. Jensen[1] · **Igor Shulman**[1] · **Hemantha W. Wijesekera**[1] · **Stephanie Anderson**[1] · **Sherwin Ladner**[1]

Received: 31 October 2016 / Accepted: 29 January 2018 / Published online: 17 February 2018
© This is a U.S. Government work and not under copyright protection in the US; foreign copyright protection may apply 2018

Abstract

Large freshwater fluxes into the Bay of Bengal by rainfall and river discharges result in strong salinity fronts in the bay. In this study, a high-resolution coupled atmosphere-ocean-wave model with comprehensive physics is used to model the weather, ocean circulation, and wave field in the Bay of Bengal. Our objective is to explore the submesoscale activity that occurs in a realistic coupled model that resolves mesoscales and allows part of the submesoscale field. Horizontal resolution in the atmosphere varies from 2 to 6 km and is 13 km for surface waves, while the ocean model is submesoscale permitting with resolutions as high as 1.5 km and a vertical resolution of 0.5 m in the upper 10 m. In this paper, three different cases of oceanic submesoscale features are discussed. In the first case, heavy rainfall and intense downdrafts produced by atmospheric convection are found to force submesoscale currents, temperature, and salinity anomalies in the oceanic mixed layer and impact the mesoscale flow. In a second case, strong solitary-like waves are generated by semidiurnal tides in the Andaman Sea and interact with mesoscale flows and fronts and affect submesoscale features generated along fronts. A third source of submesoscale variability is found further north in the Bay of Bengal where river outflows help maintain strong salinity gradients throughout the year. For that case, a comparison with satellite observations of sea surface height anomalies, sea surface temperature, and chlorophyll shows that the model captures the observed mesoscale eddy features of the flow field, but in addition, submesoscale upwelling and downwelling patterns associated with ageostrophic secondary circulations along density fronts are also captured by the model.

Keywords Air-sea interaction · Submesoscale flows · Coupled atmosphere-ocean modeling · Ocean modeling · Fronts · Eddies

1 Introduction

Ocean color images from space have revealed the existence of submesoscale variability characterized by spiral eddies, squirts, cusps, and filaments. They occur in zones of strong current shear, in island wakes, and in regions with strong tides. Ocean gliders, which measure vertical profiles of the upper ocean temperature and salinity every few hours along transects that can extend hundreds of kilometers, have revealed substantial variability at submesoscales wherever they are deployed.

Submesoscale variability grows rapidly in cases where local winds are aligned with currents along a density front. In that case, submesoscale motions lead to frontogenesis or, through mixed layer instabilities, to restratification of the upper ocean depending on local wind direction relative to density gradients (Thomas et al. 2008). Restratification tends to leave density-compensated fronts behind and reduces the observed mixed layer depth, an effect that only is captured in models that resolve or parameterize submesoscale motions (Lévy et al. 2010). Submesoscale eddies have much stronger spatial gradients and much larger vertical velocities than mesoscale fronts (e.g., Mahadevan and Tandon 2006; Thomas et al. 2008; Sarkar et al. 2016). As a result, the submesoscale features have enhanced stirring which suggests there is more mixing than at mesoscales (D'Asaro et al. 2011).

Just a decade ago, basin-scale ocean circulation models only had sufficient resolution to permit mesoscale eddies

---

This article is part of the Topical Collection on the *48th International Liège Colloquium on Ocean Dynamics, Liège, Belgium, 23-27 May 2016*

Responsible Editor: Ananda Pascual

✉ Tommy G. Jensen
Tommy.Jensen@nrlssc.navy.mil

[1] Oceanography Division, Code 7320, U. S. Naval Research Laboratory, Stennis Space Center, MS 39529, USA

and subgrid scale parameterizations specific for mesoscale flows, and submesoscale flows were only studied in idealized models. In contrast, modern regional coupled atmosphere-ocean models can now be used at high resolutions that permit inclusion of at least part of the submesoscale flows and scalar quantities as will be demonstrated in this work. In a fully coupled atmosphere-ocean system simulation of a realistic geographical region, we can expect the interaction between the air and sea to increase the submesoscale energy compared to an uncoupled ocean forced by surface fluxes with low temporal and spatial resolution. In this study, it is the objective to show illustrative examples of the submesoscale processes that can be found when a submesoscale permitting ocean model is coupled directly to a high-resolution atmospheric model and wave model in order to give the reader an idea of rich phenomena that can be found and of the potential for future research on submesoscale air-sea interaction in realistic models.

An important phenomenon discovered in satellite scatterometer observations within the last few decades is a strong positive correlation between wind speed and SST on mesoscales (e.g., Chelton et al. 2004). High local SSTs lead to high local wind speeds due to reduced stability of the atmospheric boundary layer. In the vicinity of a SST front (i.e., warmer and cooler SSTs are on each side of the front causing a density gradient), this mechanism leads to both wind stress curl and divergence, which in turn affects the front by horizontal and vertical advection. In contrast, if the same ocean density front is due to salinity differences, then no feedback to the atmosphere occurs. The air-sea interaction on submesoscales is likely similar to the coupling on mesoscales although that remains to be demonstrated.

Also, locally generated waves on each side of a SST front will experience different wind forcing and have different wave heights and, hence, a different roughness across the front providing a different feedback to the submesoscale motions. The oceanic spatial submesoscales are of the same order as convective cumulus clusters and squall lines, which allow for strong air-sea interactions.

Consequently, in order to simulate scales ranging from a few kilometers to a few tens of kilometers, a high-resolution modeling system that includes air-sea interaction through coupling as well as surface waves is required. Increased capability in computing resources is now allowing “submesoscale permitting” coupled models of regional seas. To our knowledge, previous work has not been done using a fully coupled atmosphere-ocean-wave model to investigate the interaction of oceanic submesoscale features with wind waves, tides, mesoscale mixed layer currents, and the feedback to the local wind and atmospheric boundary layer. As stated above, the aim of this paper is to explore some of the oceanic features that can be simulated in such a coupled model rather than provide a comprehensive study. In spite of the smaller spatial scales and large vertical motions, hydrostatic models with resolutions of 500 m to 1 km are adequate to realistically model many of these features, specifically the vertical heat and salinity flux in the upper ocean (e.g., Mahadevan 2006). Advances in computational resources and state-of-the-art coupled models like COAMPS make it possible to address these issues for the first time.

1.1 The Bay of Bengal

It was noted above that oceanic density fronts often are subject to submesoscale activity. Over the Bay of Bengal (BoB), the local precipitation is large, about 1100 km^3 per year as is the runoff from surrounding land areas. Including the major rivers Brahmaputra, Ganges, and Irrawaddy, the total freshwater input is 4050 km^3 annually (e.g., Sengupta et al. 2006; Jensen et al. 2016). The large freshwater source results in a shallow low-salinity surface layer imbedded in a mixed layer with higher salinity below. The outflow of low-salinity water near the surface must be balanced over longer time scales by a subsurface inflow of high-salinity water into the southern Bay of Bengal with large annual exchange rates depending on the monsoon season (e.g., Jensen 2001; Wijesekera et al. 2015; Jensen et al. 2016). This results in the occurrence of numerous very sharp salinity fronts throughout the bay, and as recently observed using profiling wire-walkers, these salinity fronts induce large variability of the upper ocean on spatial submesoscales (Lucas et al. 2016). The focus of this paper will be on the role of low-salinity water and salinity fronts on submesoscales in the ocean-atmosphere system in the Bay of Bengal. A comprehensive overview of the oceanography and air-sea interaction in the Bay of Bengal can be found in Schott and McCreary (2001) and Schott et al. (2009). A recent special issue of *Oceanography* (e.g., Mahadevan et al. 2016) includes observations and idealized modeling studies of submesoscale activity in the Bay of Bengal.

2 Methods

2.1 Coupled atmosphere-ocean modeling

The coupled modeling system consists of three modeling modules: the Coupled Ocean-Atmosphere Mesoscale Prediction System (COAMPS), the Navy Coastal Ocean Model (NCOM), and Simulating Waves Nearshore (SWAN) system. The methodology to couple the three modules was developed at the Naval Research Laboratory (NRL). COAMPS-NCOM-SWAN provides ocean simulations that are fully coupled (or uncoupled) where the ocean circulation is forced by surface fluxes that feed back to the atmospheric boundary layer and includes the effects of surface waves. The air-sea coupling is needed to provide realistic and consistent high-frequency and high wavenumber ocean surface forcing.

In the model simulations included in this paper, COAMPS is applied with a number of nested grids with different resolutions. COAMPS has been used and validated over for the Indian Ocean during MJO events in boreal spring of 2009 (Shinoda et al. 2013) and during boreal fall of 2011 during the Dynamics of the Madden-Julian Oscillation (DYNAMO) experiment (Chen et al. 2016; Jensen et al. 2015).

2.2 Atmospheric model

Until recently, COAMPS referred to a limited area atmospheric model used for research and operational forecasts by the U.S. Navy (Hodur 1997; Chen et al. 2003). The system includes a comprehensive atmospheric analysis system (Goerss and Phoebus 1992) that employs the NRL Atmospheric Variational Data Assimilation System (NAVDAS) to assimilate a wide range of surface, radiosonde, and satellite meteorological observations (Langland and Baker 2004). The data assimilation ensures an atmosphere-ocean state where the large-scale and mesoscale circulation and vertical temperature and moisture profiles are close to reality during the model integration.

The analysis uses a 0.5° × 0.5° grid and 30 vertical levels. COAMPS was set up as described below. The atmospheric model covers the Bay of Bengal region over an area of about 5400 km × 2700 km using a Mercator projection centered on 90° E, 0° N, extending from 66° E to 102° E and from about 2° S to 26° N. The model uses up to three atmospheric grids with two-way nesting. The resolution is 18 km on the coarse grid (208 × 168 grid points). An inner nest covering 69° E to 99° E, 1° S to 23° N has a resolution of 6 km (502 × 424 grid points); in one case, an inner 2 km nest is used. All atmospheric grids use 60 levels in the vertical and the time step is 40 s for the coarser grid.

2.3 The ocean model

NCOM was developed at NRL by Martin (2000). The model has a hybrid sigma-z vertical coordinate and a free surface. It was originally based on the Princeton Ocean Model (POM) by Blumberg and Mellor (1987) and has many aspects common with POM. For instance, it is using the same C-grid layout, the same equation of state (Mellor 1991), and the same 2.5 level turbulent closure scheme for vertical mixing (Mellor and Yamada 1982) modified by Kantha and Clayson (2004) to include Stokes drift from the surface wave model. A notable difference is the treatment of the barotropic mode. NCOM employs a semi-implicit scheme that uses a preconditioned conjugate gradient solver for the resulting elliptic equation, whereas POM uses an explicit scheme with time-splitting. NCOM is also using improved numerical schemes such as fourth-order calculation of Coriolis and pressure gradients and third-order advection (Holland et al. 1998). The model includes monthly climatological river runoff (Barron and Smedstad 2002) with 41 discharge locations in the Bay of Bengal and around Sri Lanka and 8 major diurnal and semi-diurnal tidal constituents (K1, O1, P1, Q1, K2, M2, N2, and S2) based on the methodology of Egbert et al. (1994) and Egbert and Erofeeva (2002). Surface wave radiation stress is included from the wave model. A single grid covers the ocean model on a spherical grid using a resolution of 1/54° on a 1600 × 1320 grid with a time step of 30 s. There are 60 vertical levels: 45 sigma levels with 15 z-levels below depths of 330 m.

2.4 SWAN spectral wave model

The SWAN wave model covers the same area as the ocean model, but with 1/8° spatial resolution using 33 frequency bands for wave periods between 1 and 24 s and an angular resolution of 7.5°, i.e., 48 wave directions. The time step is 60 s. We use third-generation mode wave physics with Komen linear wave growth model including the Cavaleri and Malanotte-Rizzoli (1981) growth term, quadruplet interaction, and whitecapping (Komen et al. 1984), with the formulation of wave dissipation by Rogers et al. (2012). To reduce the garden-sprinkler effect (e.g., Booij and Holthuijsen 1987), which is associated with the finite spectral resolution, a diffusive wave age time scale of 12 h is applied. Forcing is 10 m wind from the atmosphere model and the free surface currents (0 m depth) from the ocean model.

2.5 Initial conditions and boundary conditions

The regional atmospheric model gets its initial and boundary conditions from the global atmospheric models, either the Navy Operational Global Atmospheric Prediction System (NOGAPS) for dates before April 1, 2013, or the Navy Global Environmental Model (NAVGEM) after that date and from observations available at The Fleet Numerical Meteorology and Oceanography Center (FNMOC). The atmospheric model is initialized using quality-controlled observations from surface stations, ships, radiosondes, aircraft, and satellites and from a 12-h global forecast with a spatial resolution of 0.5° × 0.5° available at FNMOC. The observations and the global forecasts are analyzed using NAVDAS and projected onto the atmospheric forecast model grids. The boundary conditions provided by the global atmosphere model are updated every 6 h.

The ocean model is initialized and its boundaries are forced every 6 h by output from the 1/8° global NCOM with 40 vertical levels (Barron et al. 2006) for runs before 2013 and by output from the 1/12° global Hybrid Coordinate Ocean Model (HYCOM) for recent model runs (Metzger et al. 2014). Outside the active ocean model area, the SST used to compute fluxes to the atmosphere model is from the Navy

Coupled Ocean Data Assimilation (NCODA) analysis (Cummings 2005). This is standard setup for COAMPS when run without an active ocean.

2.6 Coupling between atmosphere and ocean in COAMPS

Surface fluxes are computed in the atmospheric model and the two model components exchange flux information using the Earth System Modeling Framework (ESMF, www.earthsystemmodeling.org) software infrastructure developed by the National Center for Atmospheric Research (NCAR). Sea surface temperature is passed from the ocean model to the atmosphere model, and forcings to the ocean model are wind stress components, precipitation, net surface heat flux, and short wave radiation. The latter is provided independently to compute penetrative radiation into the ocean. All fluxes are interpolated to the coarsest ocean grid. The ocean model SST is used by the atmospheric model to calculate upward long wave radiation, sensible heat flux, and latent heat flux. A bulk parameterization using the boundary layer formulation by Louis (1979) is used. For additional details see Jensen et al. (2011). A coupling interval of 6 min was used for the coupled model runs presented here. Figure 1 illustrates the communication between the different model components. The atmosphere forecast model and ocean model codes used domain decomposition and run in parallel using the message passing interface (MPI), which makes the couple model system run fast and efficient on distributed memory computer architectures.

The coupled model is run with a 12-h update cycle. The result of an atmospheric and ocean analysis that includes data assimilation is used as initial condition for a 12-h forecast. For subsequent forecasts, the analysis uses the previous forecast as a first guess for the analysis, i.e., the atmospheric state will assimilate new observations into a model/data synthesis before the next 12 h forecast. The ocean model is not using any data assimilation in the interior, but along the boundaries through the data assimilation employed by global NCOM or HYCOM.

2.7 Satellite observations

A Group for High Resolution Sea Surface Temperature (GHRSST) level 4 daily data are produced daily on an operational basis by the Naval Oceanographic Office (NAVOCENO), with ~ 10 km resolution. This global SST analysis uses multiple satellite data and in situ data from drifting and moored buoys. GHRSST data are downloaded from ftp://podaac-ftp.jpl.nasa.gov/OceanTemperature/ghrsst/data/L4/GLOB/NAVO/K10_SST/.

Level-1B imagery from the Suomi National Polar-orbiting Partnership (SNPP) Visible Infrared Imaging Radiometer Suite (VIIRS) was processed to level 2 (sensor grid), 3 (mapped grid), and 4 (composites) using the Naval Research Lab's Automated Processing System (APS) (http://www7333.nrlssc.navy.mil/docs/aps_v6.4/html/user/aps.xhtml). APS estimates chlorophyll-a by the OCI algorithm (Hu et al. 2012) at 0.75 km pixel resolution. The diffuse attenuation coefficient Kd (488) was estimated in accord with (Lee et al. 2005). The Kd (488) was used to estimate the euphotic depth (noted Eu); the Eu was estimated as the depth where photosynthetic available radiation (PAR) is 1% of its surface value (Lee et al. 2007):

$$\mathrm{Eu} = -\ln(0.01)/\mathrm{Kd}(488)$$

The merged all satellite global ocean gridded sea level anomalies (SLA) L4 data is downloaded from the Copernicus Marine Environment Monitoring Service **(**http://marine.copernicus.eu/services-portfolio/access-to products/?option=com_csw&view=details&product_id=SEALEVEL_GLO_SLA_MAP_L4_NRT_OBSERVATIONS_008_026). Each SLA level 4 gridded data product is collected over a 7-day period and the spatial resolution is 0.25° × 0.25°.

3 Results

3.1 Submesoscale generation by precipitation

Observations of the effect of tropical rainfall in the Western Pacific have been investigated in previous research (Smyth et al. 1996a, b; Wijesekera and Gregg 1996; Wijesekera et al. 1999) and by idealized modeling studies (Wijesekera et al. 2003). In the modeling work, it was demonstrated that surface trapping of momentum and inhibition of turbulence below the freshwater lens occurred, and upwelling and downwelling occurred along the upwind and downwind edges of the salinity anomaly, respectively. The scale of the rain event was 30 km resulting in mesoscale currents. In this work, similar tropical rain events are examined, but under more realistic conditions simulated in a coupled atmosphere-ocean model.

In COAMPS, the atmospheric forcing over the ocean changes every 6 min, and the length scales in the atmospheric boundary layer are small. In this simulation, three atmospheric nests are used: 18, 6, and 2 km. In particular, convective systems are explicitly modeled, although not well resolved. Strong downdrafts result in strong divergent winds, and associated heavy precipitation occurs on the grid scale in the atmospheric model and is able to generate submesoscale motion in the ocean. The ocean model has a 4.5-km grid and a 1.5-km inner nest allowing the latter to resolve submesoscales. Figure 2, left panel, shows the 10-m wind associated with an intense rain event over a location in the southern part of the Bay of Bengal. The figure shows the wind field in every third grid point in each direction after 9 h of the forecast started at

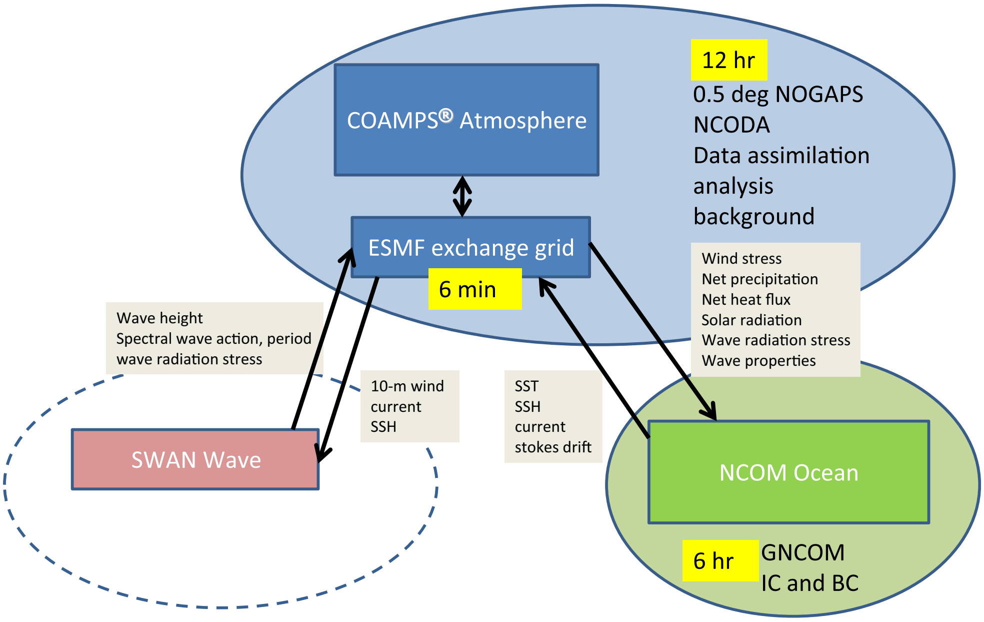

Fig. 1 Coupled Ocean-Atmosphere Mesoscale Prediction System setup and data exchange

April 1, 1200 UTC. Forecast hours mentioned below are counted from that time. Before the onset of the storm, the mean surface wind is northeasterly and remains in that direction north of 7.5° N. South of that is an area of convective clouds where heavy rain and strong downdrafts develop. Local winds exceed 12 m/s and the total rainfall over a 12-h period exceeds 100 mm (Fig. 2, right panel). The convective rain is moving into the area from the northwest with heavy rainfall 8 h into the forecast. Several distinct precipitating cells in the interior of the area lower the surface salinity and drive divergent surface currents. Figure 3 shows the response hour by hour in the ocean, starting at 1800 UTC, or 6 h into the forecast (Fig. 3a). The initial surface currents are westward. At 2100 UTC, a wake is generated behind the main center of precipitation (Fig. 3d). The northwestward current developing during 1900–2000 UTC (Fig. 3b, c) does not appear to be directly wind driven but suggestively looks like a wake behind the low-salinity lens. After 2100 UTC (Fig. 3d), the first major rain event is over, and the freshwater lens is diluted by mixing. At hour 2300 UTC, 11 h into the forecast (Fig. 3f), a new

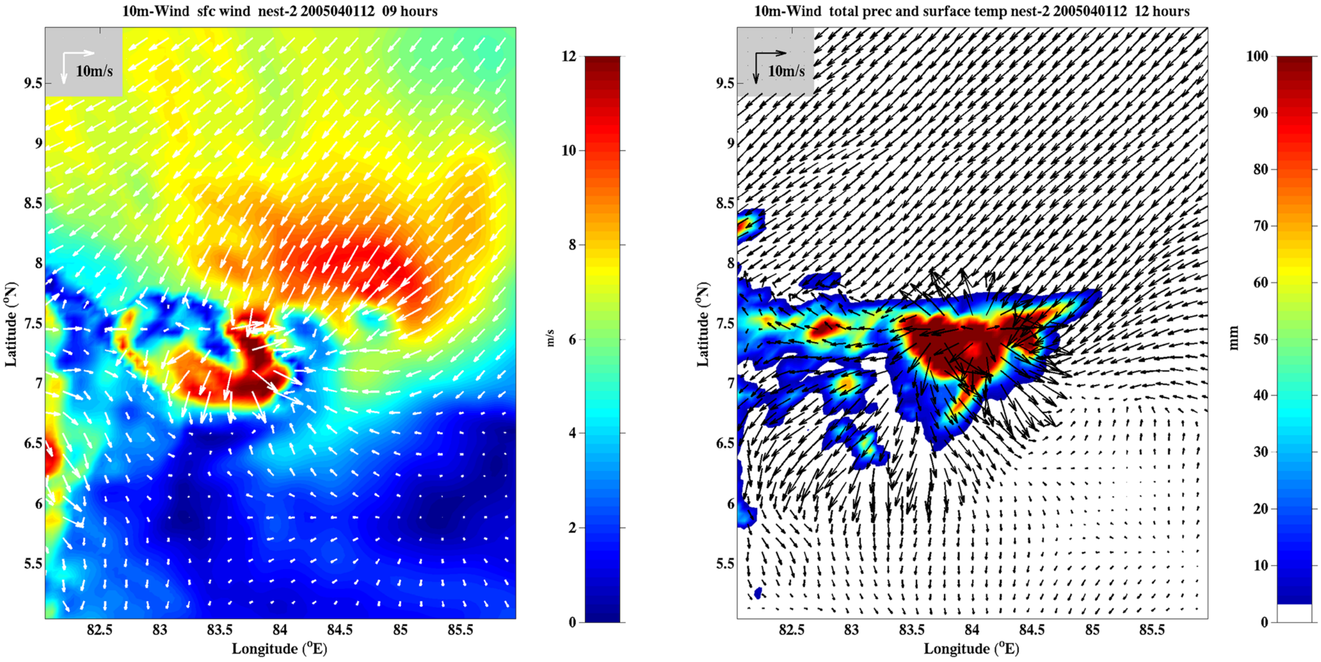

Fig. 2 Vectors of 10-m winds and wind speed (color) on April 1 at 2100 UTC (left); 10-m wind vectors and 12 h accumulated precipitation on April 2 at 0000 UTC (right)

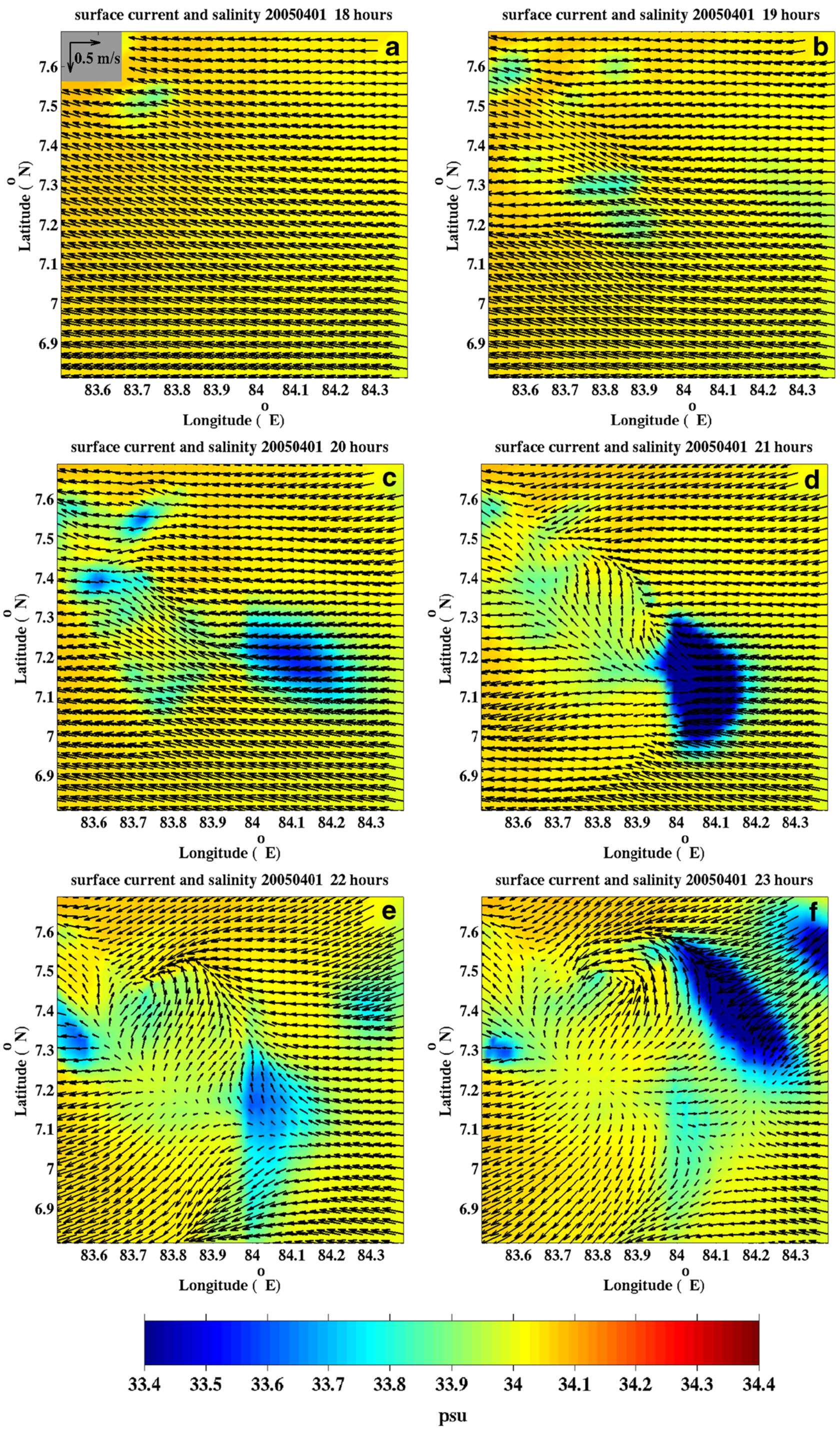

Fig. 3 **a**–**f** Hourly surface currents and surface salinity from a rain event over the southern Bay of Bengal starting on April 1 at 1800 UTC, 2005

major rain event develops to the northeast. These submesoscale and mesoscale currents are intermittent, last several hours after each precipitation event stops, but subsequent convective clusters force new current systems on the scales of the atmospheric convection. Vertical cross sections (Fig. 4) along 84.1° E are through the center of the largest freshwater lens. Figure 4, top, shows the salinity and meridional velocity component on the 1.5-km ocean grid and on the 4.5-km ocean grid (Fig. 4, bottom). The solutions on both grids show spreading of the freshwater anomaly with advection away for the center of the lens, i.e., northward advection on the northern edge and southward advection on the southern edge. The divergent currents cause upwelling under the freshwater lens and downwelling associated with the spreading freshwater front. During the storm, an intensified northeasterly local wind north of 7.5° N drives a predominantly south-

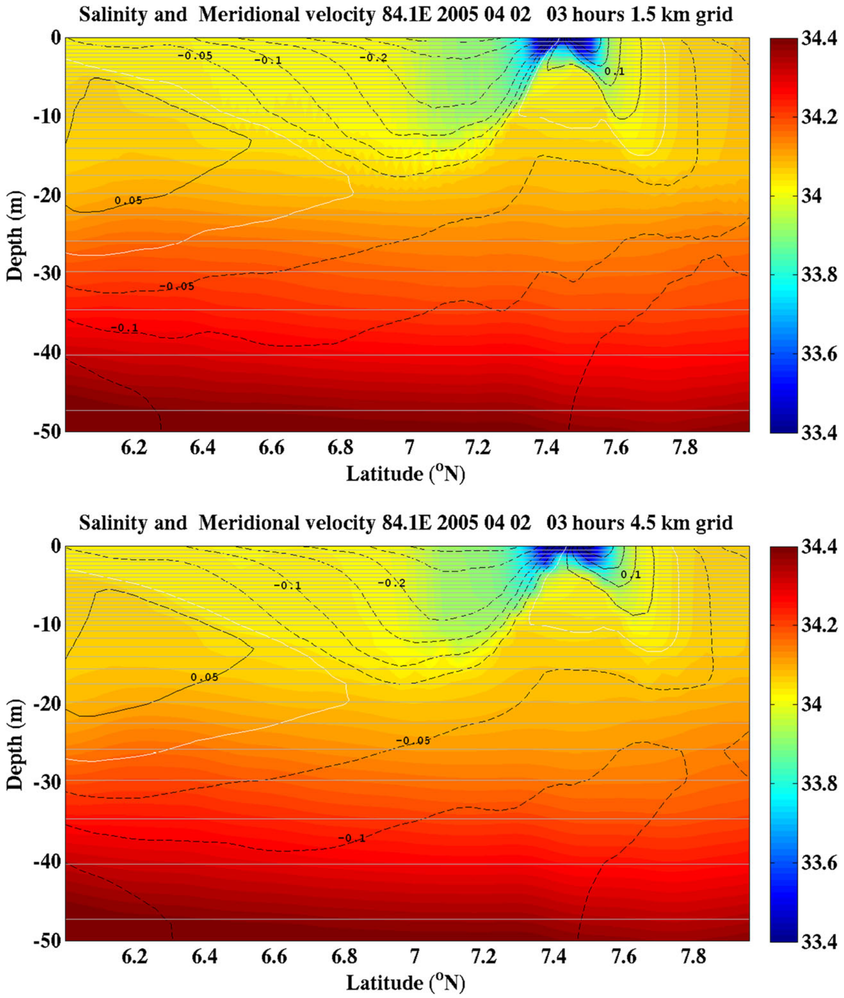

Fig. 4 Vertical section of salinity (color) and meridional velocity (contours) on April 2 at 0300 UTC, 2005, from 1.5 km ocean model grid (top) and 4.5 km ocean model (bottom). Contour interval is 0.05 m/s. Negative contours are dashed, positive contours are solid lines. Zero contour is white. The horizontal gray lines show the location of the vertical grid in the model

westward local current, opposing the northward advection north of the lens and enhances the southward freshwater advection to the south. A day later, the salinity in the center of the freshwater lens has mixed with upwelling salinity water, resulting in a local salinity maximum. This can be seen in Fig. 5 that shows the currents and salinity at 15 m on April 3, at 0900 UTC. While not needed to see the local salinity maximum, a spatial high-pass filter has been applied to remove large-scale features so the difference between the 1.5-km ocean grid (Fig. 5, top) and the 4.5-km grid (Fig. 5, bottom) is more clearly seen. The high-pass-filtered field is the difference between the original field and the low-pass smoothed field using a simple spatial moving average over 15 grid points in east-west and over 15 grid points in the north-south directions.

Before the rainfall event, the mesoscale dynamics are very similar for both ocean nests. The 1.5-km nest shows larger vertical halocline displacements and that smaller horizontal scales are present compared to the 4.5-km solution (Figs. 4 and 5). The overall effect of the higher resolution at this time is small, except that instability develops along a salinity front near 85° E, 6° N.

The early mesoscale response to the two first rain events is very similar for the two ocean grids (Fig. 4). However, after 10 days with five major rain events, a drop in salinity of about 0.2 psu in the upper 25–30 m north of 6.7° N are seen in both model solutions. The high-resolution 1.5-km nest (Fig. 6, upper panel) has significantly higher larger spatial variations in halocline depth and shows an increased thickness of the upper low-salinity layer. Between 6.4° N and 6.7° N, the salinity in the mixed layer is significantly lower in the 1.5-km grid (nest 2) than in the 4.5-km grid solution (Fig. 6, lower panel). That is due to eastward advection of low-salinity water in nest 2, a feature that is absent in the coarser nest. It is also noteworthy that the salinity gradient in the upper 20 m near 6.5° N is significantly stronger in the 1.5-km grid solution (Fig. 6, top) with a meridional velocity in excess of 0.45 m/s. In the 4.5-km grid solution (Fig. 6, bottom), the front is weaker and meridional currents are less than 0.2 m/s.

The ability to model the collective effect of successive rainfall events in a realistic system is the main advantage using a fully coupled modeling system, and using an ocean model

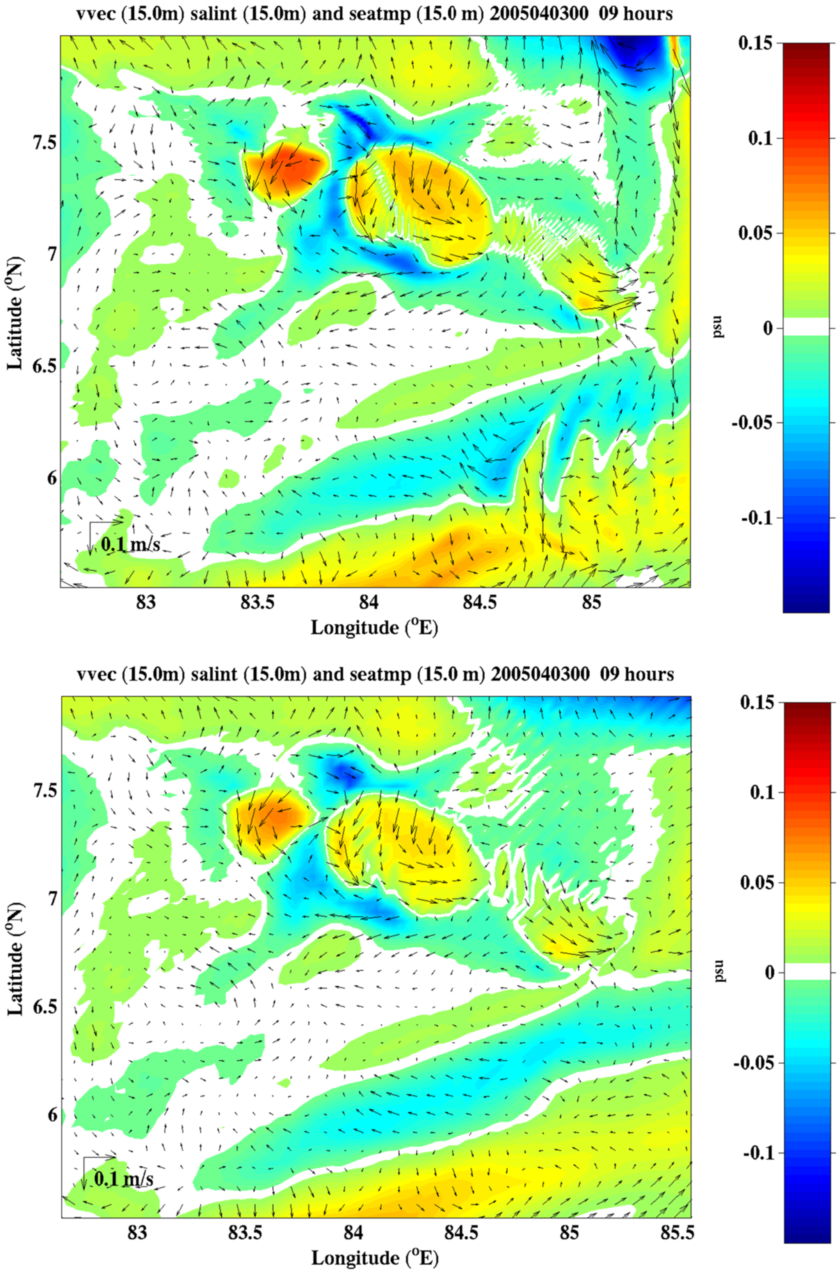

Fig. 5 High-pass-filtered currents and salinity at 15 m on April 3 0900 UTC on the 1.5-km ocean grid (top) and on the 4.5-km ocean grid (bottom)

that permits submesoscale oceanic scales can have an impact on the mesoscales as shown here.

3.2 Submesoscale generation near fronts

Barotropic tides generally have large scales in the open ocean; however, interaction with bottom topography produces internal tides and internal waves with tidal periods. A prime example of this mechanism is found in the Andaman Sea (e.g., Jackson 2004, 2007). For this case, the horizontal resolutions in the atmosphere and ocean models are 6 and 2 km, respectively. Surface waves are included with a resolution of 13 km. The model experiment was done as follows. A fully coupled run was performed using a 6-min coupling interval with diurnal and semidiurnal tides included, and the surface meteorology and surface fluxes were stored at hourly intervals. This surface forcing was then used to run two coupled ocean-wave model simulations. One included tides, the other did not. It was necessary to run an uncoupled run to isolate the effects of tides. Running a fully coupled model with and without tides will lead to two different atmospheric feedback scenarios within a few days, and the forcing of the ocean will differ due to different air-sea interactions.

Figure 7 shows the zonal currents in the Bay of Bengal with distinct divergence and convergence patterns from semidiurnal solitary internal waves radiating from the gaps in the

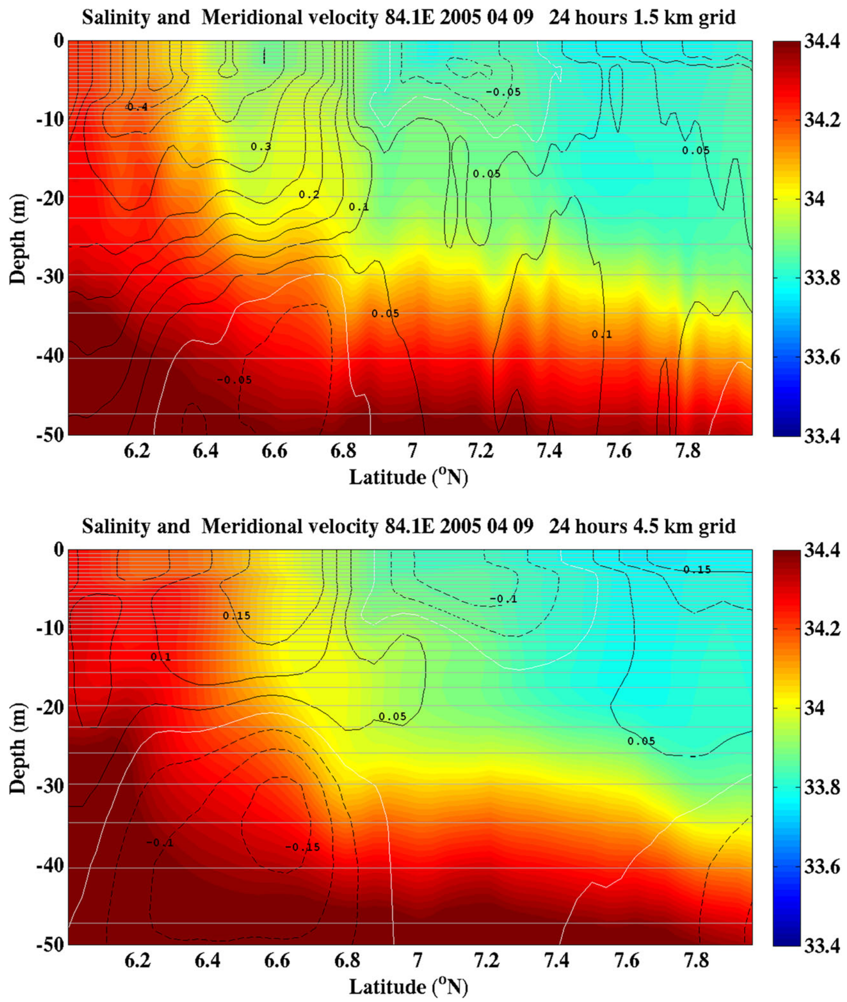

Fig. 6 Vertical section of salinity (color) and meridional velocity (contours) on April 10 at 0000 UTC, 2005. Solutions are shown on the 1.5-km ocean grid (top) and on the 4.5-km ocean grid (bottom). Contour interval is 0.05 m/s. Negative contours are dashed, positive contours are solid lines. Zero contour is white. The horizontal gray lines show the location of the vertical grid in the model

Andaman Sea Archipelago where the waves are generated by flow over the sills (Jackson et al. 2012). The waves can propagate over long distances with little interference with the large-scale mean flow. However, they can interact with submesoscale flow anomalies and modify flow on small scales as demonstrated in this section. The distance between wave fronts is about 100 km and a new wave arrives every 12.4 h at a given location. The semidiurnal waves have been found in recent observations of temperature salinity and chlorophyll in the Bay of Bengal (e.g., Lucas et al. 2016). The width of a front is about 6 km in the model, which is the same scale as the resolved submesoscale features.

High-salinity water is flowing from the Arabian Sea into the Bay of Bengal as a strong eastward flow past the southern tip of Sri Lanka during the southwest monsoon (Fig. 7). Surface currents exceed 1 m/s and there is a strong lateral current shear along sharp density fronts along the northern edge of the intrusion (e.g., Wijesekera et al. 2015; Jensen et al. 2016). The daily average wind speed in the area is above 9 m/s and persistently from the southwest. The pattern of convergence and divergence in the zonal velocity field is produced by the semidiurnal solitary waves emanating from the Andaman Sea.

Interference between these waves and the northern front of the intruding Arabian Sea water will be examined in this section.

Figure 8 (top panel) shows the zonal current component (color shading) and sea surface salinity contours along the northern salinity front. It is from a model run without tides. Frontal instability is a generation mechanism for submesoscale features along fronts (e.g., Mahadevan and Tandon 2006; Thomas et al. 2008). The front in Fig. 8 is subject to submesoscale velocity and salinity perturbations as is evident in the figure. The mean current at the surface is from the south and is advecting denser, high-salinity water toward the front (Fig. 8, top). It is also seen that there is convergence along the front, an indication that the higher salinity water is subject to subduction along the front. This was confirmed by examining vertical sections across the front as shown below.

The two lower panels show the flow anomalies and salinity anomalies on small scales after the large spatial scales have

Fig. 7 Instantaneous surface currents (vectors) and zonal velocity component (color) on September 1, 2011, at 0000 UTC. The color scale is chosen to emphasize a change in the sign in the zonal velocity component. Solitary waves are generated as the semidiurnal tides flow over the relatively shallow sills in the Andaman Sea Archipelago

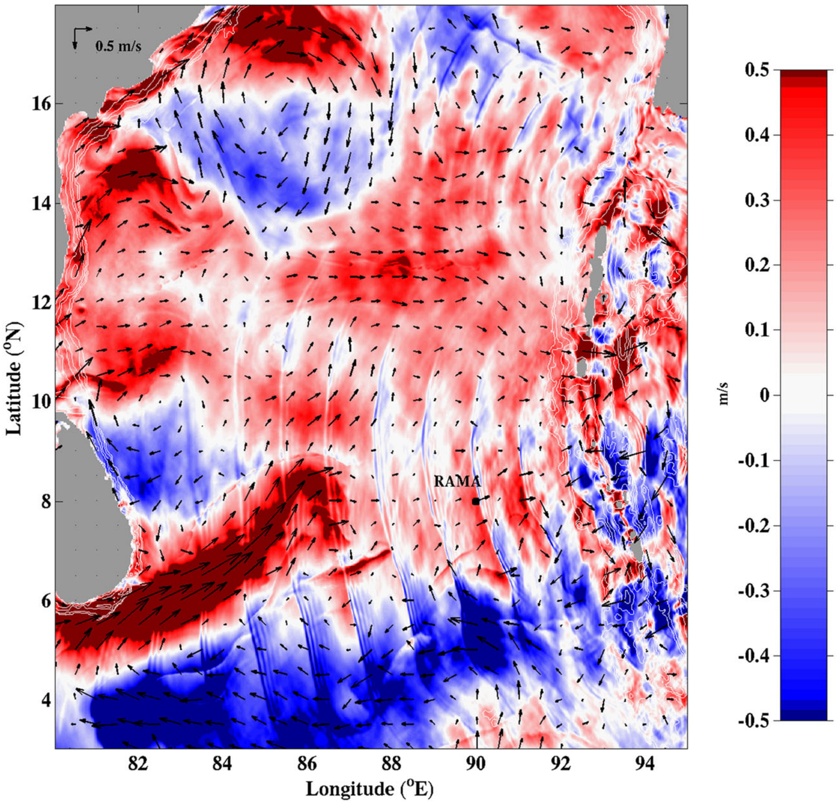

been removed. A 15-point wide spatial running average is done both in east-west and in north-south directions to produce large-scale fields of velocity components and salinity. The high-pass spatial component of each variable is produced by subtraction the smoothed field from the original field.

The center panel shows the small-scale spatial anomalies of the flow and salinity in the upper panel. There are cyclonic eddy anomalies along the front with a diameter of about 10 km. The small-scale flow along the northern edge of the front is against the wind with a tendency to advect lower salinity water toward the front. In the solution shown in the top and center panels, the tides were not active, so the semidiurnal solitary waves seen in Fig. 7 are not present in the model solution. Figure 8, bottom panel, shows the filtered solution when tides are included. Enhanced westward zonal flow anomalies seen near 84.8° E and 85.9° E are aligned south to north and are due to the solitary waves. The vertical structure of the meridional current and salinity across the anticyclonic anomaly flow from Fig. 8 (bottom panel) is shown in Fig. 9. The upper panel shows the unfiltered meridional velocity component and salinity with the main front located at 8.5° N. Low-salinity water is to the north, extending from the surface to a depth of about 20 m. The lower panel shows the anomaly fields after removing the large horizontal scales. Note that there is convergence in the mixed layer and divergence along the base of the mixed layer (Fig. 9, lower panel). The contours for salinity (Fig. 9, top) also indicate subduction on the south side of the front. Using the velocity convergence rates and scales in Fig. 9, an estimate of subduction of 40 m/day is found. A very similar subduction scenario has been simulated in an idealized shallow salinity front using stratification and forcing from the Bay of Bengal (see Fig. 6 in Sarkar et al. 2016). The role of the submesoscale anomaly circulation is a cross-front transport of freshwater and salt: It enhances subduction and northward flow of high salinity below the halocline to the north of the front and southward transport of negative salinity anomalies to the south.

Compared to the case without tides, the submesoscale eddies along the front are intensified in the tidal case and the front is weaker than without tides. The solitary waves have strong convergence and divergence patterns on a small scale as seen in Fig. 7. This scale is on the same order as the submesoscale meanders along the front and modulates the cyclonic eddy motion along the front. The daily averaged flow fields look very similar to the instantaneous fields in Fig. 8. Computations of 3-day averages show that when tides are included, the salinity front is weaker than in the case without tides, implying a stronger cross-frontal salinity transport. In Fig. 10, upper panel, that shows the model solution without tides, a coherent area with salinity anomalies above 0.1 psu is seen along the front between 84.1° E and 84.8° E. The cyclonic motion generated by the submesoscale instability is present after 3 days averaging both with and without tides, but stronger with tides present (Fig. 10, lower panel).

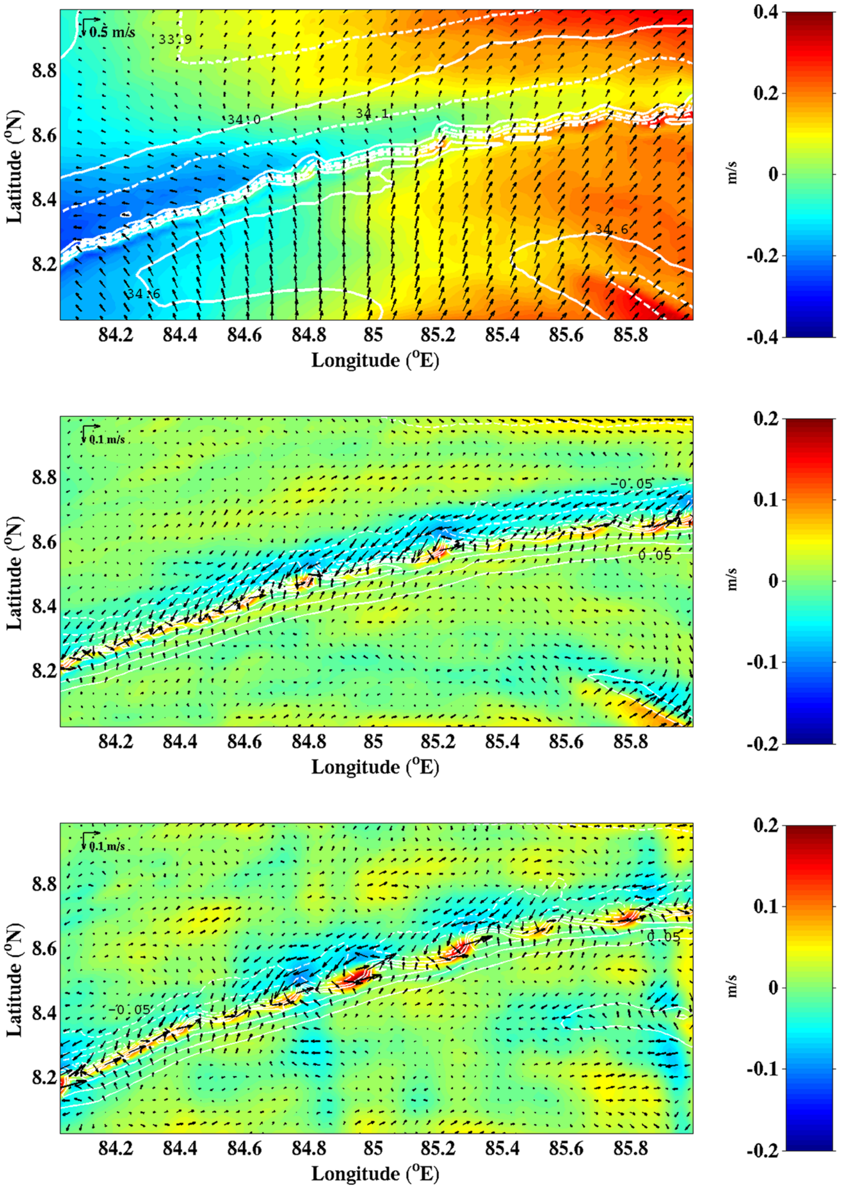

Fig. 8 Surface current vectors and magnitude of zonal current velocity (color) and salinity (contours) of the unfiltered flow on August 29 at 1800 UTC (top). The contour interval is 0.1 psu with alternating full and dashed contour lines. Anomalies of the same quantities of the spatial high band pass-filtered flow from a run without tides (center). The bottom panel shows the filtered solution with tides included. Contour interval 0.05 psu for filtered results and dashed/full lines for negative/positive values

3.3 Dynamics of observed submesoscale filaments with elevated chlorophyll content

In previous studies (Shulman et al. 2015), it was demonstrated that submesoscale processes supported and modulated the development of satellite-observed submesoscale chlorophyll-a filaments in the areas of interaction between cold upwelled water and warm offshore anticyclonic circulation. Similar elevated chlorophyll-a submesoscale filaments extending offshore of the Godavari River delta are present in the satellite ocean color imagery in the western part of the Bay of Bengal (Fig. 11). Our objective is to investigate whether submesoscale processes contributed to the local processes that maintained the observed streaky chlorophyll-a filaments offshore of the Godavari River for more than 2 weeks.

On April 10, the elevated chlorophyll-a filament extends offshore for more than 3° of longitude from the delta of the Godavari River. The filament is about 10–20 km across, and it follows the northern edge of the warm anticyclonic circulation as seen in the GHRSST image for April 10 of 2016 (Fig. 12). This warm anticyclonic circulation is formed by the East India Coastal Current (EICC) flowing along the coast and offshore and bringing warmer water from the south during the pre-Southwest monsoon (March–April, see Shetye et al. 1993; Gomes et al. 2000). Nine days later, on April 19, the chlorophyll-a filament (Fig. 11) again follows the edge of the warm and more defined anticyclonic circulation (which penetrates deeper offshore) (Fig. 12). Then, the filament turns around offshore and moves onshore along the edge of another warm anticyclonic circulation to the north, as seen in the GHRSST image (Fig. 12). Remarkably, the filament persists

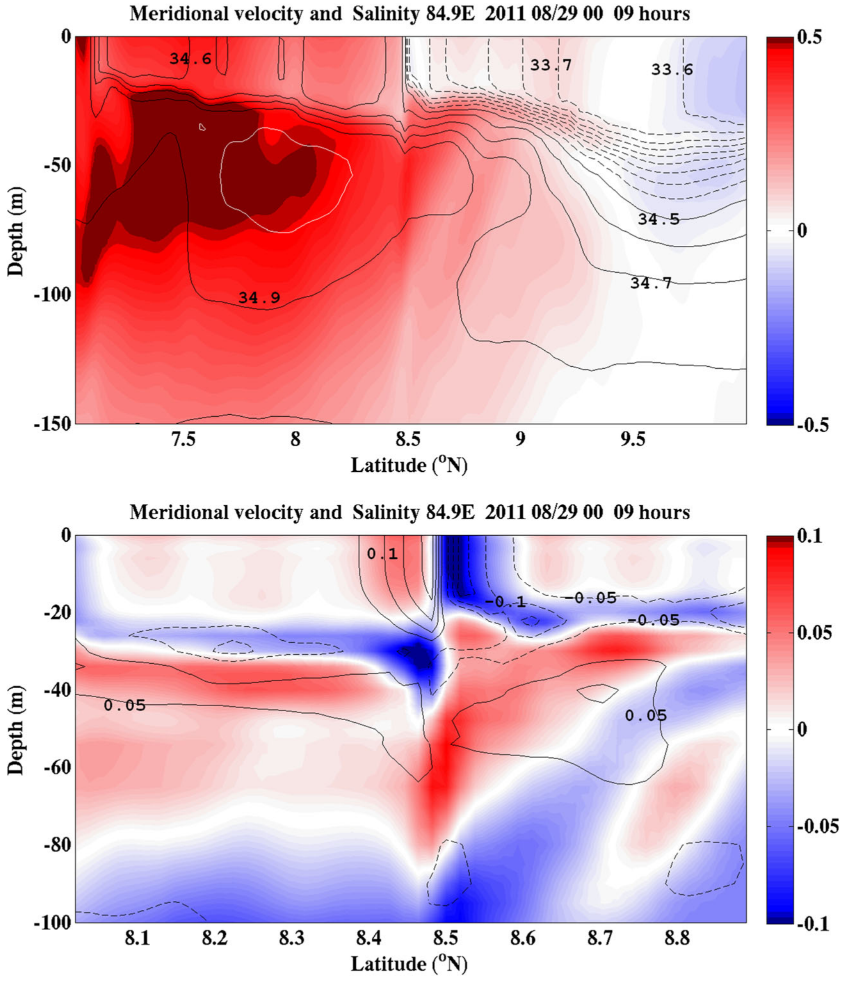

Fig. 9 Vertical cross section along 84.9° E the meridional current velocity (color, unit m/s) and salinity (contour) for the run with tides on August 29 at 0900 UTC. Contour interval is 0.1 psu with dashed line < 34.5 and solid lines above. White contour indicates 35.0 psu (top). Lower panel shows the meridional velocity anomaly (color) and salinity anomaly (contours) near the strong salinity front after filtering out the large horizontal scales. Contour interval for salinity is 0.05 psu. Note the difference in latitude range and depth range between the two panels

in the VIIRS images a week later, during April 25–28. Satellite GHRSSTs (Fig. 11) and the SLA maps (Fig. 12) show that the filament follows the edges of two warm anticyclonic circulations with cyclonic circulation between them. The SLA maps in Fig. 13 are based on 7-day observation periods and are downloaded from Copernicus Marine Environment Monitoring Service.

Figure 11 shows that the filament is connected to the high chlorophyll water masses close to the coast, and it is likely that the advection of relatively high chlorophyll water masses from the area close to the coast along the edge of the warm anticyclonic circulation contributed to the development of the observed submesoscale filament. However, the filament with elevated chlorophyll-a content persists for more than 2 weeks, and it extends offshore for more than 300–400 km. In this situation, it is likely that processes local to the filament contribute to the growth and maintenance of the phytoplankton population and elevated chlorophyll-a values for such an extended time. As demonstrated above, the filament is located in the frontal areas between mesoscale features: warmer mesoscale anticyclonic circulations interacting with the colder inshore water and with meandering along the coast and offshore EICC current. In such cases, it is known that submesoscale processes can contribute to the development and maintenance of narrow, streaky chlorophyll filaments (Lévy et al. 2012; Mahadevan and Archer 2000; Mahadevan and Tandon 2006; Calil and Richards 2010; Shulman et al. 2015).

To investigate if submesoscale processes contributed to the maintenance and development of the observed filament, we use COAMPS with horizontal resolutions of 6 km in the atmosphere and 2 km in the ocean, respectively. Both surface waves and tides are included as well.

Figures 14, 15, and 16 show the model daily averaged SSTs, SSH, and currents fields during the considered time frame. Visual comparisons of observations (Figs. 12 and 13) and model results (Figs. 13 and 14) show that the model includes the major mesoscale features presented in satellite observations: meandering along the coast and offshore current (resembling EICC current); this current brings warmer water from the south and forms the warm anticyclonic circulation; there is development of the second warm anticyclonic circulation to the north. As a result of assimilation of SSTs from multiple satellites, the model SSTs (Fig. 14) resemble GHRSSTs (Fig. 12) well. There is a very good match between

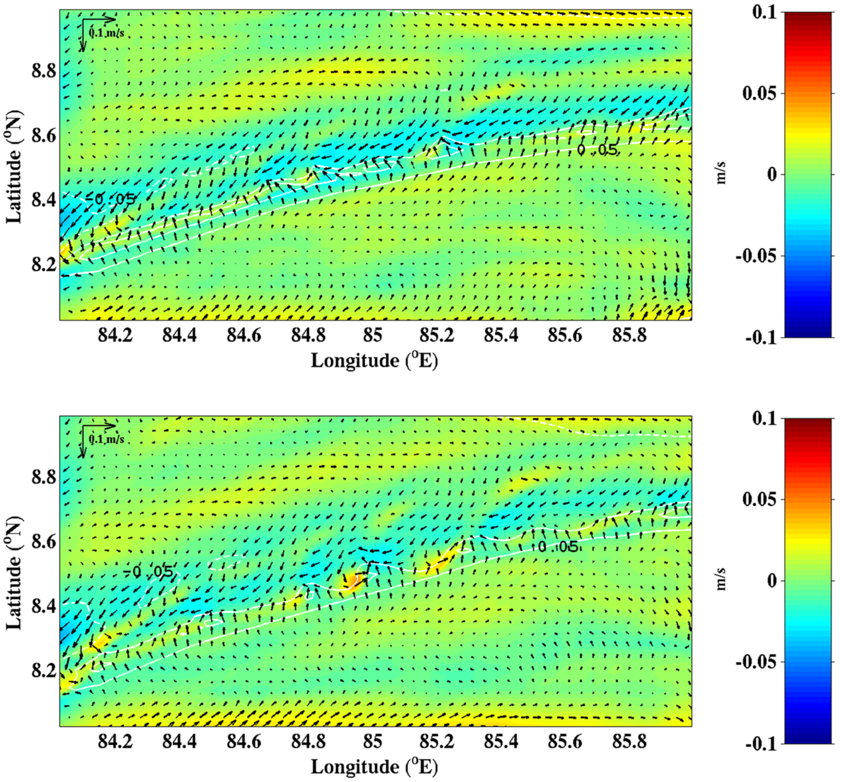

Fig. 10 Filtered surface current vectors and magnitude of zonal current velocity (color) and salinity (contours) averaged over 72 h from August 28 through August 30 for the case without tides (top) and the case with tides (bottom). Note that the scales of the vectors and the color scale are different than in Fig. 8. Contour interval is 0.05 psu with dashed/full lines for negative/positive values. The zero contour is not shown

model and observations at the location of the edge of the warm anticyclonic circulation close to the Godavari River delta (or the match in location of the EICC current flowing offshore of the Godavari River delta). However, this warm eddy (or EICC current) penetrates much further offshore in the observations than in the model results on April 20 and 26. The center of the cyclonic eddy (between two anticyclonic circulations, Fig. 13) and the interaction with the warmer eddy to the north are further offshore in observations than in the model. As a result, the location of the observed filament matches the inshore location of the warm eddy edge in the model. However, the observed offshore turn of the filament and migration onshore does not match the location of mesoscale features in the model. In spite of differences in positioning of mesoscale features in the model, the presence of the major observed mesoscale and frontal structures in model predictions provides the possibility to evaluate interaction of these features and the contribution of submesoscale processes to maintaining the observed elevated chlorophyll-a filament, especially in areas where the model features match the observed.

Interaction of the warm anticyclonic circulation with the colder upwelled inshore water leads to the development of

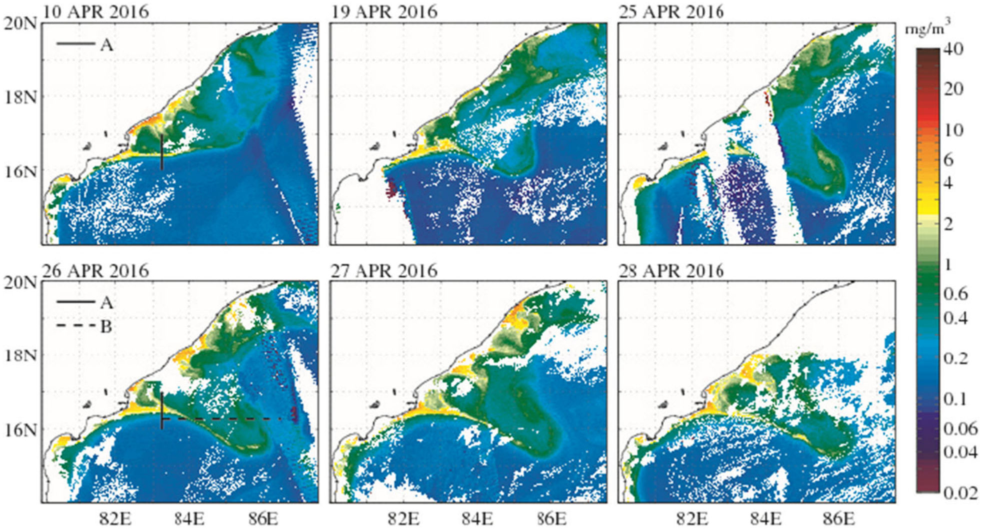

Fig. 11 Chlorophyll-a based on satellite VIIRS ocean color imagery with locations of sections A and B on selected days in April 2016. Unit is milligrams per liter

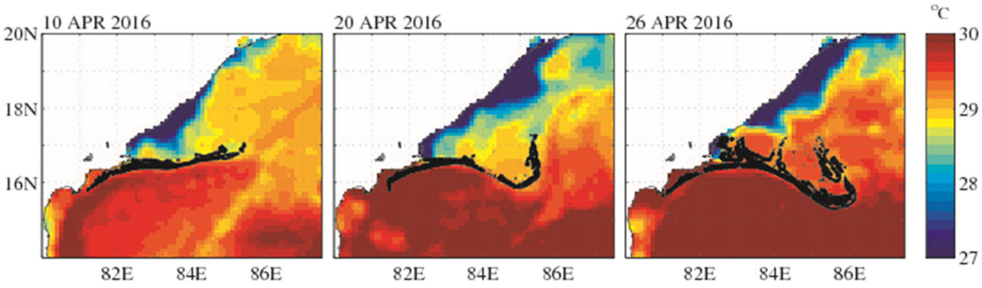

Fig. 12 Satellite GHRSST on April 10 (left), April 20 (center), and April 26, 2016 (right). Unit is degree Celsius. Locations of submesoscale filaments are shown in black

the surface frontogenesis with ageostrophic secondary circulation (ASC) cells generated in the plane perpendicular to the density front with upwelling on the light side of the front and downwelling on the dense site of the front (Hoskins 1982; Lévy et al. 2012; Calil and Richards 2010; Shulman et al. 2015).

In Hoskins (1982), the vector Q_1 is used to qualitatively diagnose ageostrophic vertical motion due to frontogenesis:

$$Q_1 = \left(-\frac{\partial u_g}{\partial x}\frac{\partial b}{\partial x} - \frac{\partial v_g}{\partial x}\frac{\partial b}{\partial y}, -\frac{\partial u_g}{\partial y}\frac{\partial b}{\partial x} - \frac{\partial v_g}{\partial y}\frac{\partial b}{\partial y} \right) \quad (1)$$

Where $u_g$and v_g are the horizontal geostrophic velocities, and $\frac{\partial b}{\partial x}$ and $\frac{\partial b}{\partial y}$ are the horizontal gradients of buoyancy:

$$b = -g\frac{\rho^*}{\rho_0} \quad (2)$$

with ρ^* being the deviation from the reference density ρ_0, and g is the acceleration due to gravity. The local maximum of Q_1 creates a vertical circulation with associated upwelling/downwelling ASC cells.

Figure 17 shows the observed and modeled-predicted properties plotted along the sections crossing the submesoscale filament (Fig. 11). The isothermal layer depth (ITLD) is computed as the depth at which temperature deviates by 0.3 °C from the temperature at the 2-m reference level. Correspondingly, the isopycnal layer depth (IPLD), which we also call the mixed layer depth (MLD), is defined as the depth where a density change corresponds to 0.3 °C temperature change. Our sensitivity studies of ITLD and IPLD estimations by using different values for the reference level (5 or 10 m) and with a temperature difference of 0.2 °C produced results similar to the case when the reference level is 2 m and the temperature difference is 0.3 °C. The barrier-layer thickness (BRLD) is computed as the difference between the ITLD and IPLD, BRLD = ITLD − IPLD.

In Fig. 17a, the observed VIIRS chlorophyll-a, ITLD, IPLD, BRLD, euphotic depth (Eu), and the vector Q_1 magnitude (1) are shown along section A crossing the filament (Fig. 11). The values of ITLD, IPLD, BRLD, and Q_1 were estimated based on the 48-h averaged model fields of temperature, salinity, and velocity, centered on April 10 00Z. Estimated values of Q_1 were averaged over the top 50-m depth. There is well-defined local maximum in the magnitude of the vector Q_1, which is shifted to less than 0.2° (20 km) from the observed location of the submesoscale filament (chlorophyll maximum on Fig. 17a). This can probably be explained by the before mentioned fact that the locations of major mesoscale features (like edges of warm anticyclonic circulation and position of EICC) are shifted in the model (Figs. 14 and 15) in comparison to the observed locations (Figs. 12 and 13). The local maximum of Q_1 magnitudes creates a vertical circulation with associated upwelling/downwelling ASC cells (Hoskins 1982). ASC cells are upward (upwelling) on the light (warm anticyclonic) side of the front and downward on the dense side of the front. Figure 17a indicates that the ITLD and IPLD are shallower than the estimated euphotic depth (Eu). In this case, the developed ASC cells kept phytoplankton in the lighted area and supported photosynthesis and phytoplankton growth. Also, the BRLD layer is very thin (almost equals to 0, Fig. 17a) in the area of filament; therefore, there is no salinity layer preventing ASC cells in providing injections and cycling of nutrients into the euphotic area and facilitating the consumption of

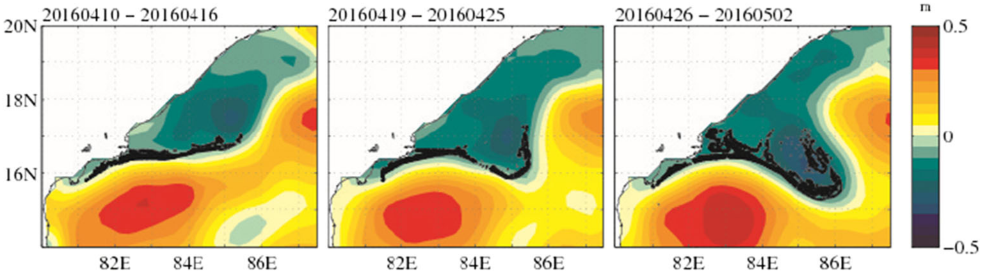

Fig. 13 Observed mean sea level anomaly over 7-day periods from merged global ocean altimeter data. Each 7-day observation period is ending on April 16 (left), April 25 (center), and May 5, 2016 (right). Locations of submesoscale filaments are shown in black

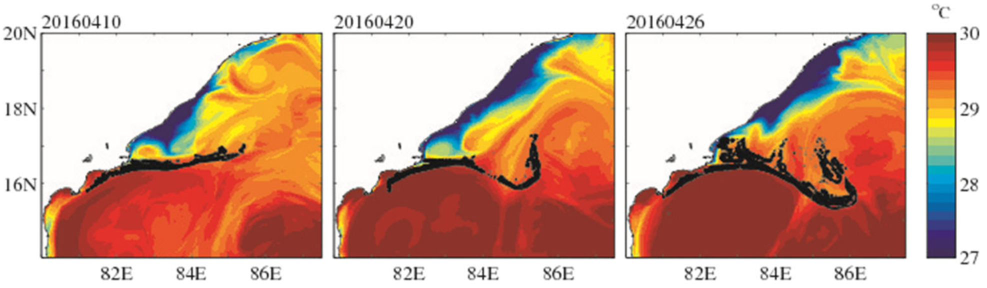

Fig. 14 Sea surface temperature from COAMPS on April 10 (left), April 20 (center), and April 26, 2016 (right). Unit is degree Celsius. Locations of submesoscale filaments in the observations are shown in black

nutrients (however, we do not have observations supporting this).

On April 26th, Fig. 17b, c shows a good match in locations of the local maximum of Q_1 with the chlorophyll-a maximum along section A and at the first inshore crossing of the filament by section B (Fig. 11). The coincidence of Q_1 and chlorophyll maxima together with the presence of very shallow BRLD layers in the area of chlorophyll maxima, and with the fact that IPLD and ITLD are shallower than the euphotic layer depths around the filament, supports the conclusion that the surface frontogenesis modulated phytoplankton growth in the observed submesoscale filament.

Figure 16 (right panel) shows a mismatch between the location of the second maximum in Q_1 and the location of the second chlorophyll maximum at the second (more offshore) crossing of the filament by section B (Fig. 11). This is a result of the before discussed mismatches in offshore locations of observed and model-predicted mesoscale features.

In the area of EICC, currents are ~ 1.5 m/s (Fig. 16). With a horizontal scale of filament ~ 300 km, the scale of advection is ~ 2.3 days. MLD in the model is ~ 25–30 m (Fig. 17), and with the model vertical velocity ~ 10^{-4} m/s (Figs. 18 and 19), the scale of ASC cells is ~ 3 days. Therefore, advection and ASC cells had similar time scales during the observed submesoscale filament.

Figure 18 (bottom) shows the vertical velocity at 20 m depth on April 26, 2016. The intense eastward flow around 16° N of the southern anticyclonic eddy turns sharply southward as it reaches a north-south-aligned salinity front near 84.5° E (Fig. 18, top). At the front, large downward vertical velocities are found (Fig. 18, bottom panel). The convergence is also evident from the currents in the salinity plot in the upper panel in the same figure. Salinity water of about 33.5 psu is subducting under lower salinity water of about 32.5 psu. Cross sections of 24 h averaged vertical velocity along 16° N and 16.5° N (Fig. 19) show that there is subduction at the front in an area near 84° E, 16° N to at least 100 m while upwelling is seen in an area at the front around 84.5° E, 16.5° N. These vertical velocities are consistent with the surface currents in Fig. 18 (top) that show convergence and divergence, respectively, at those two locations. The presence of the vertical motion to depths of 100 m and deeper along the frontal zone is of significant importance for vertical mixing in the Bay of Bengal.

Feedback to the atmosphere from the ocean is included on mesoscales. Figure 20 shows the heat surface heat flux on April 10, 2016, and the surface wind stress. When compared to SST (Fig. 14), it is seen that the ocean is gaining heat over cold anomalies and being cooled over warm SST. The effect of SST and wind stress on mesoscales as reported by Chelton et al. (2004) can be seen in Fig. 20 as well. The wind stress has a local minimum over the cold SST and the heat flux is downward. The atmospheric model resolution is 6 km and does not resolve the oceanic submesoscales so it is unknown if the same feedback mechanism is active on that scale.

3.4 Summary and conclusions

The simulation of the ocean circulation of the Bay of Bengal by COAMPS resolves mesoscale features and is also able to capture part of the submesoscale phenomena in its ocean model component. It was demonstrated that precipitation from convective cumulus in the atmospheric model directly can force submesoscale flows in the upper ocean. Localized rainfall and associated convection and strong downdrafts are usually not available when prescribed atmospheric forcing is used

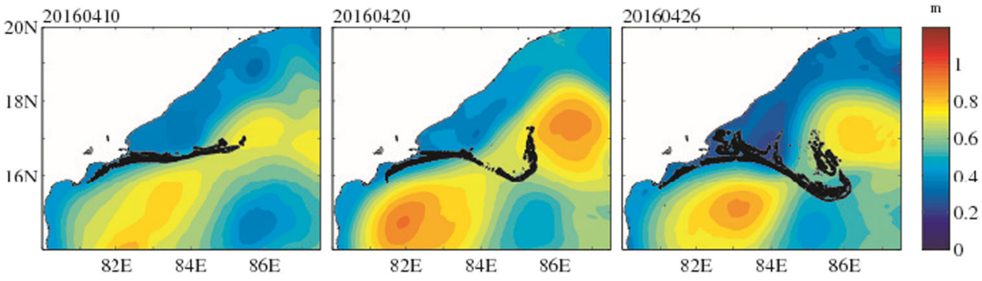

Fig. 15 Sea surface height from COAMPS on April 10 (left), April 20 (center), and April 26, 2016 (right), computed as a 25-h average. Locations of observed submesoscale filaments are shown in black

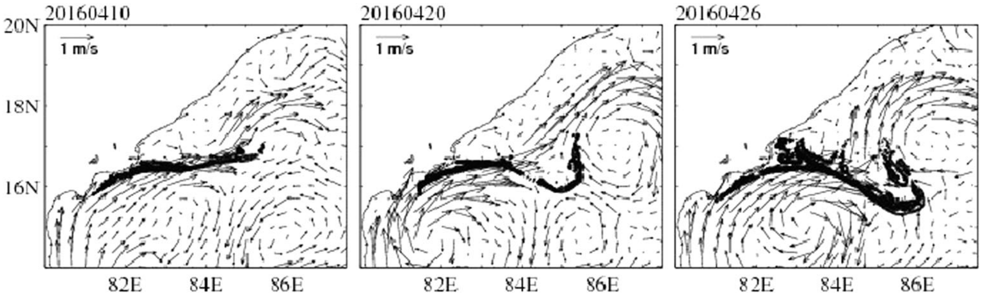

Fig. 16 Surface currents from COAMPS on April 10 (left), April 20 (center), and April 26, 2016 (right), computed as a 49-h average. Locations of observed submesoscale filaments are shown in black

for ocean models, but are readily available in a coupled system with frequent air-sea coupling. Consequently, a coupled model has the potential for generation of more submesoscale features. The low-salinity lenses typically last for several hours and, under calm conditions, for longer than a day. The horizontal spreading of the low-salinity water lenses induces a vertical circulation that reaches the base of the mixed layer. In our case study, the cumulative effect of convective rain on the ocean is a deepening of the mixed layer and lowering its salinity. We found that vertical displacements of the halocline had larger amplitudes and had smaller spatial scales in the 1.5-km ocean model compared to the 4.5-km ocean model and fronts were sharper. That can be expected given the increased resolution. The reason for increased vertical mixing with higher horizontal resolution is not clear. The subsurface ocean model output was saved in 3-hourly snapshots, so a careful

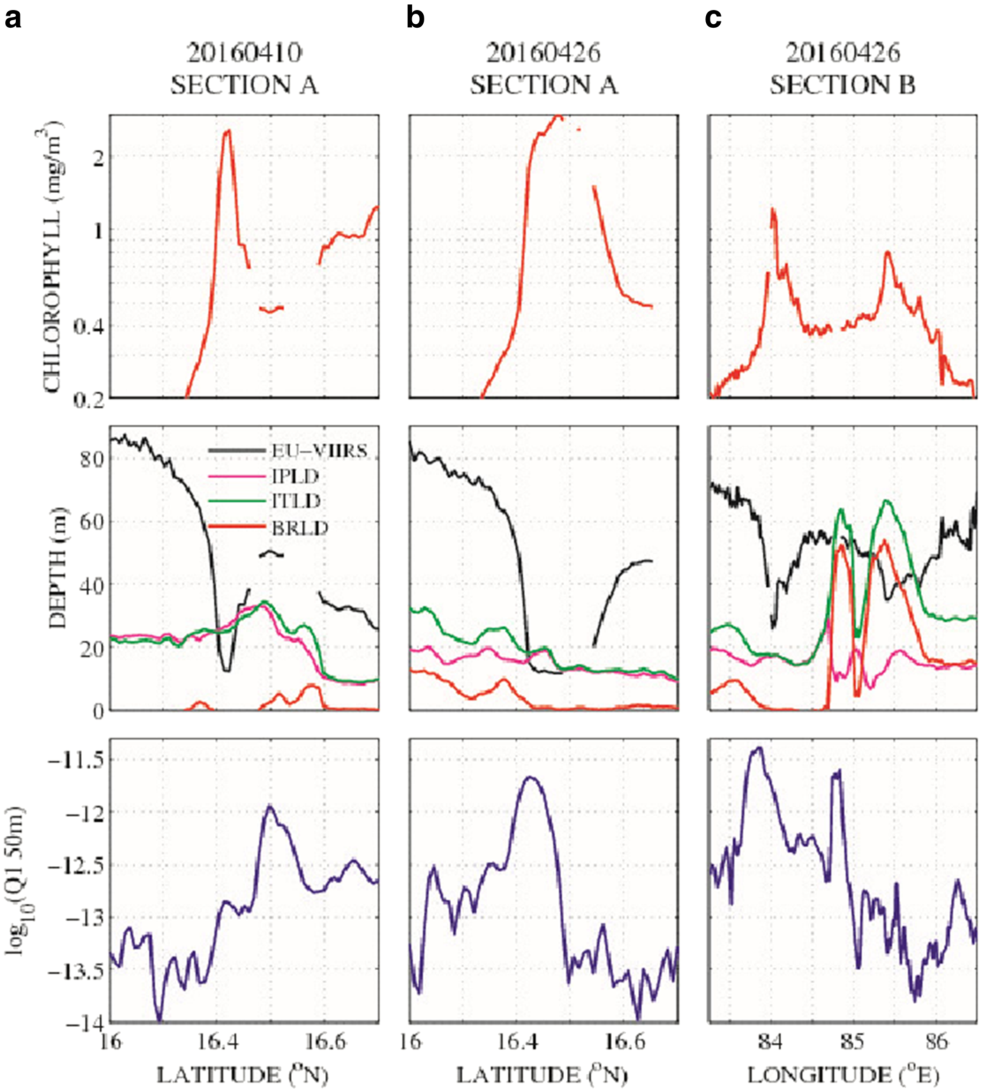

Fig. 17 Observed and model-predicted properties plotted along sections crossing the submesoscale filaments (Fig. 11): **a** section A on April 10, **b** section A on April 26, and **c** section B on April 26. Top panels: VIIRS chlorophyll-a along the section; middle panels: euphotic depth (black), isopycnal layer depth (IPLD; magenta), isothermal layer depth (ITLD; green), and barrier layer thickness (BRLD; red); bottom panels: magnitude of the Q1 vector

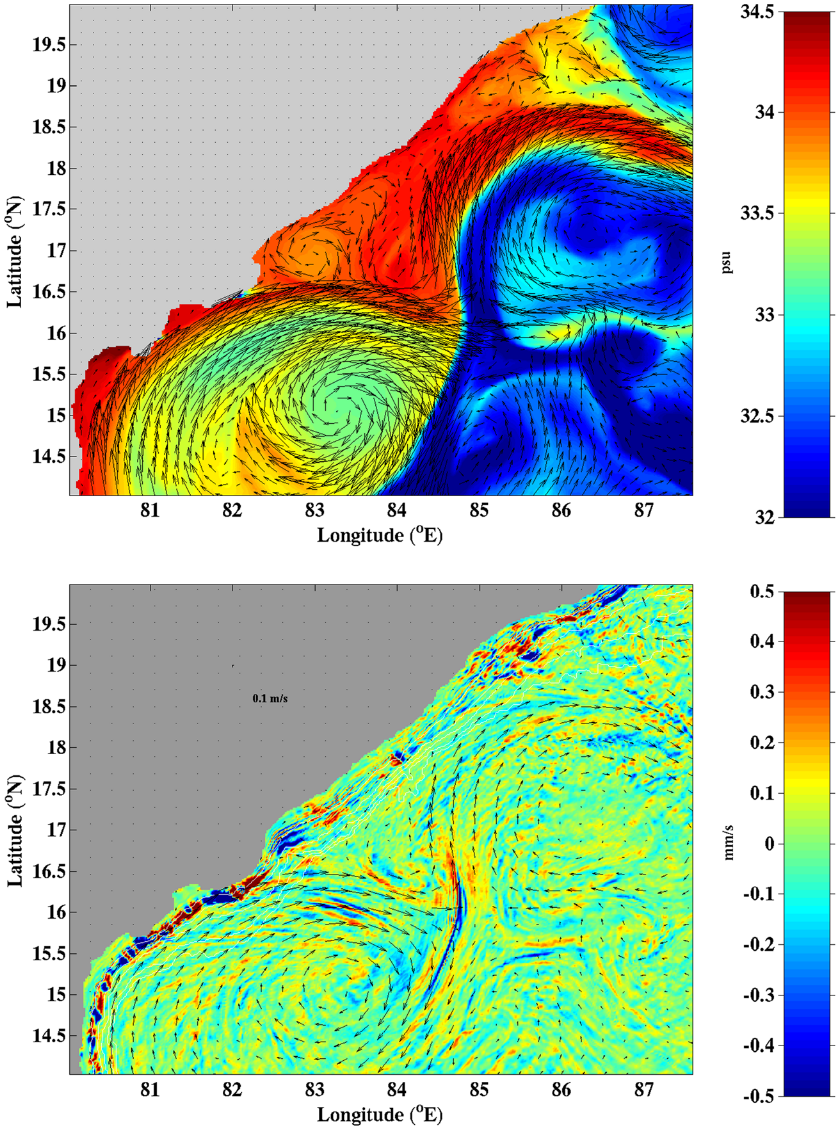

Fig. 18 Surface current and surface salinity (top) and 20-m current and vertical velocity (bottom) averaged over 24 h on April 26, 2016. Unit is psu for salinity and 10^{-3} m/s for vertical velocity

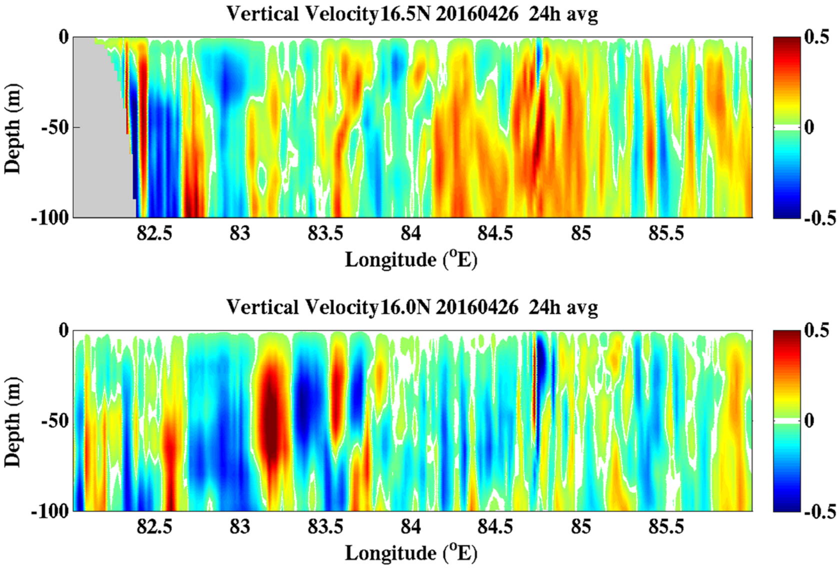
Vertical Velocity16.5N 20160426 24h avg

Vertical Velocity16.0N 20160426 24h avg

Fig. 19 Vertical velocity on April 26, 2016, average over 24 h along 16.5° N (top) and along 16.0° N (bottom). Unit is 10^{-3} m/s

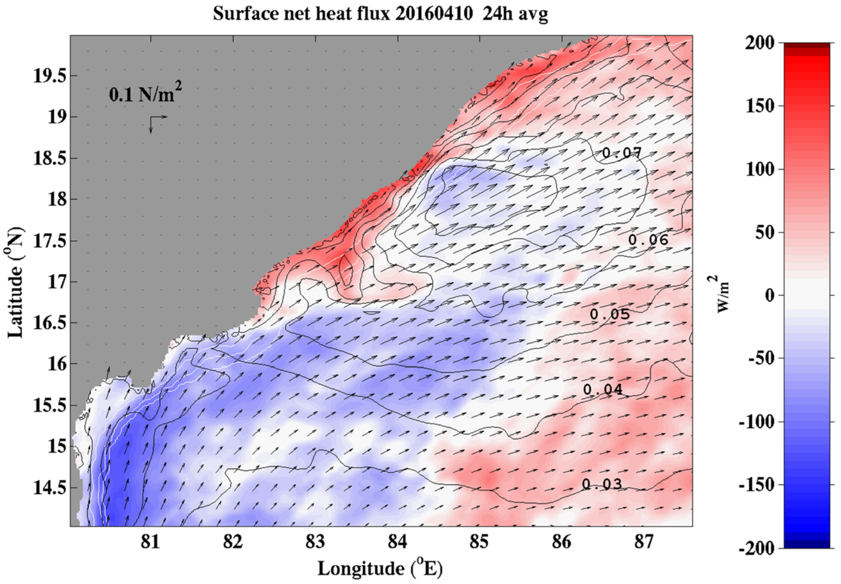

Fig. 20 Net surface heat flux (color) and surface wind stress vectors on April 10, 2016, averaged over 24 h. Heat flux into the ocean is positive, while negative heat flux is cooling the ocean. Black contours with an interval of 0.025 N/m^2 show the magnitude of the wind stress. The white contour lines along the coast show the 100-, 500-, and 1000-m isobaths

analysis cannot be made, but we speculate that there is more internal wave activity in the high-resolution case. An examination of the 3-hourly model output persistently shows larger vertical halocline displacements and variability on the 1.5-km grid (e.g., Figs. 4 and 6) and seems to be consistent with internal waves. However, the ocean model is hydrostatic, which prevents internal waves to break, so mixing from internal waves depends on the vertical mixing scheme and the numerical diffusion in the model.

The cumulative effect of higher resolution that permits submesoscale motion was shown to significantly impact the mesoscale flow. In this case, in addition to a lower salinity in the mixed layer, a near-surface front was stronger and the maximum meridional flow was increased by a factor of 2.

The ocean model resolution of 1.5 to 2 km is rather coarse for submesoscales, but the model does develop submesoscale meanders and eddies along fronts. It was found that semidiurnal solitary waves can interact with eddies at this scale and contribute to enhanced submesoscale variability. A spatial high-pass filter reveals coherent submesoscale flows along salinity gradients than enhanced salinity transports across the front. The intermittent submesoscale surface flow has very strong divergence and convergence, and it is shown that downwelling and upwelling along a strong salinity front is enhanced when both submesoscale flow and tidally induced solitary waves are included.

Satellite images of chlorophyll-a showed a persistent submesoscale filament in the vicinity of the Godavari River. An analysis of the observations and the model flow field and density field show that the model captures the mesoscale eddies—although displaced compared to eddies observed in altimetry. Based on an analysis of the ageostrophic secondary circulation and the vertical velocity field in the model, the results suggest that surface frontogenesis enabled sustained phytoplankton growth in an observed long-lived submesoscale filament.

The results from the three case studies shown in this work suggest a potential for more submesoscale activity than in an uncoupled model, primarily because of more temporal and spatial variability in the forcing from an atmosphere that is coupled very frequently to the ocean. We cannot access the feedback to the atmosphere from submesoscale oceanic temperature anomalies since the resolution in the atmospheric model is too low. It will be a topic we hope to address in the near future.

Acknowledgments We would like to thank Tim Campbell at NRL Stennis Space Center for his help with COAMPS and Jan Dastugue for the help with the graphics.

Funding information This work was supported by the US Naval Research Laboratory (NRL) 6.1 Core Program "Effects of Bay of Bengal Freshwater Flux on Indian Ocean Monsoon (EBOB)" and by the US Office of Naval Research (ONR) in an ONR Departmental Research Initiative: Air-Sea Interactions Regional Initiative (ASIRI).

References

Barron CN, Birol Kara A, Martin PJ, Rhodes RC, Smedstad LF (2006) Formulation, implementation and examination of vertical coordinate choices in the Global Navy Coastal Ocean Model (NCOM). Ocean Model 11(3–4):347–375. https://doi.org/10.1016/j.ocemod.2005.01.004

Barron CN, Smedstad LF (2002) Global river inflow within the Navy Coastal Ocean Model. Proceedings of the oceans 2002 MTS/IEEE meeting, 29–31 October 2002

Blumberg AF, Mellor GL (1987) A description of a three-dimensional coastal ocean circulation model. In: Heaps N (ed) Three-dimensional coastal ocean models. American Geophysical Union, New York, pp 347–375. https://doi.org/10.1029/CO004p0001

Booij N, Holthuijsen LH (1987) Propagation of ocean waves in discrete spectral wave models. J Comp Phys 68(2):307–326. https://doi.org/10.1016/0021-9991(87)90060-X

Calil PHR, Richards KJ (2010) Transient upwelling hot spots in the oligotrophic North Pacific. J Geophys Res 115(C2):C02003. https://doi.org/10.1029/2009JC005360

Cavaleri L, Malanotte-Rizzoli P (1981) Wind wave prediction in shallow water: theory and applications. J Geophys Res 86(C11):10961–10973

Chelton DB, Schlax MG, Freilich MH, Milliff RF (2004) Satellite radar measurements reveal short-scale features in the wind stress field over the world ocean. Science 303(5660):978–983. https://doi.org/10.1126/science.1091901

Chen S, Cummings J, Doyle J, Hodur R, Holt T, Liou C-S, Liu M, Mirin A, Ridout J, Schmidt J, Sugiyama G, Thompson WT (2003) COAMPS version 3 model description—general theory and equations. NRL/PU/7500—03-448, 143 pp.

D'Asaro ED, Lee C, Rainville L, Harcourt R, Thomas L (2011) Enhanced turbulence and energy dissipation at ocean fronts. Science 322(6027):318–322. https://doi.org/10.1126/science.1201515

Egbert GD, Bennett AF, Foreman MGG (1994) TOPEX/Poseidon tides estimated using a global inverse model. J Geophys Res 99(C12): 24821–24852. https://doi.org/10.1029/94JC01894

Egbert GD, Erofeeva SY (2002) Efficient inverse modeling of barotropic ocean tides. J Atmos Ocean Technol 19(2):183–204. https://doi.org/10.1175/1520-0426(2002)019<0183:EIMOBO>2.0.CO;2

Chen S, Flatau M, Jensen TG, Shinoda T, Schmidt J, May P, Cummings J, Liu M, Ciesielski PE, Fairall CW, Lien R-C, Baranowski DB, Chi N-H, de Szoeke S, Edson J (2016) A study of CINDY/DYNAMO MJO suppressed phase. J Atmos Sci 72:3755–3779

Cummings JA (2005) Operational multivariate ocean data assimilation. Quart J Royal Met Soc Part C 131(613):3583–3604. https://doi.org/10.1256/qj.05.105

Goerss J, Phoebus P (1992) The navy's operational atmospheric analysis. Weather Forecast 7(2):232–249. https://doi.org/10.1175/1520-0434(1992)007<0232:TNOAA>2.0.CO;2

Gomes H, Goes JI, Saino T (2000) Influence of physical processes and freshwater discharge on the seasonality of phytoplankton regime in the Bay of Bengal. Cont Shelf Res 20(3):313–330. https://doi.org/10.1016/S0278-4343(99)00072-2

Hodur RM (1997) The Naval Research Laboratory's Coupled Ocean/Atmosphere Mesoscale Prediction System (COAMPS). Mon Weather Rev 125(7):1414–1430. https://doi.org/10.1175/1520-0493(1997)125<1414:TNRLSC>2.0.CO;2

Holland WR, Chow JC, Bryan FO (1998) Application of a third-order upwind scheme in the NCAR ocean model. J Clim 11(6):1487–1493. https://doi.org/10.1175/1520-0442(1998)011<1487:AOATOU>2.0.CO;2

Hoskins BJ (1982) The mathematical theory of frontogenesis. Annu Rev Fluid Mech 14(1):131–151. https://doi.org/10.1146/annurev.fl.14.010182.001023

Hu C, Lee Z, Franz BA (2012) Chlorophyll-a algorithms for oligotrophic oceans: a novel approach based on three-band reflectance difference. J Geophys Res 117(C1):C01011. https://doi.org/10.1029/2011JC007395

Jackson, C.R. (2004) An atlas of internal solitary-like waves and their properties, 2nd ed., 560 pp. Global Ocean Assoc., Alexandria, VA (Available at http://www.internalwaveatlas.com)

Jackson CR (2007) Internal wave detection using the moderate resolution imaging spectroradiometer (MODIS). J Geophys Res 112(C11): C11012. https://doi.org/10.1029/2007JC004220

Jackson CR, da Silva JCB, Jeans G (2012) The generation of nonlinear internal waves. Oceanography 25(2):108–123. https://doi.org/10.5670/oceanog.2012.46

Jensen TG (2001) Arabian Sea and Bay of Bengal exchange of salt and tracers in an ocean model. Geophys Res Lett 28(20):3967–3970. https://doi.org/10.1029/2001GL013422

Jensen TG, Campbell TJ, Allard RA, Small RJ, Smith TA (2011) Turbulent heat fluxes during an intense cold-air outbreak over the Kuroshio extension region: results from a high-resolution coupled atmosphere-ocean model. Ocean Dyn 61(5):657–674. https://doi.org/10.1007/s10236-011-0380-0

Jensen TG, Shinoda T, Chen S, Flatau M (2015) Ocean response to CINDY/DYNAMO MJOs in air-sea coupled COAMPS. J Met Soc Japan 93A(0):157–178. https://doi.org/10.2151/jmsj.2015-049

Jensen TG, Wijesekera HW, Nyadjro ES, Thoppil P, Shriver JF, Sandeep KK, Pant V (2016) Modeling salinity exchanges between the equatorial Indian Ocean and the Bay of Bengal. Oceanography 29(2):92–101

Kantha LH, Clayson CA (2004) On the effect of surface gravity waves on mixing in the oceanic layer. Ocean Model 9:101–124

Komen GJ, Hasselman S, Hasselman K (1984) On the existence of a fully developed wind-sea spectrum. J Phys Oceanogr 14(8):1271–1285. https://doi.org/10.1175/1520-0485(1984)014<1271:OTEOAF>2.0.CO;2

Langland RH, Baker NL (2004) A technical description of the NAVDAS adjoint system. NRL/MR/7530-04-8746. Naval Research Laboratory, Monterey

Lee ZP, Darecki M, Carder KL, Davis CO, Stramski D, Rhea WJ (2005) Diffuse attenuation coefficient of downwelling irradiance: an evaluation of remote sensing methods. J Geophys Res 110(C2):C02017. https://doi.org/10.1029/2004JC002573

Lee ZP, Weidemann A, Kindle J, Arnone R, Carder KL, Davis C (2007) Euphotic zone depth: its derivation and implication to ocean color remote sensing. J Geophys Res 112(C3):C03009. https://doi.org/10.1029/2006JC003802

Lévy M, Klein P, Tréguier A-M, Iovino D, Madec G, Masson S, Takahashi K (2010) Modifications of gyre circulation by submesoscale physics. Ocean Model 34(1-2):1–15. https://doi.org/10.1016/j.ocemod.2010.04.001

Lévy M, Ferrari R, Franks PJS, Martin AP, Rivière P (2012) Bringing physics to life at the submesoscale. Geophys Res Lett 39:L14602. https://doi.org/10.1029/2012GL052756

Louis J-F (1979) A parametric model of vertical eddy fluxes in the atmosphere. Bound Layer Meteor 17(2):187–202. https://doi.org/10.1007/BF00117978

Lucas AJ, Nash JD, Pinkel R, MacKinnon JA, Tandon A, Mahadevan A, Omand MM, Freilich M, Sengupta D, Ravichandran M, Le Boyer A (2016) Adrift upon a salinity-stratified sea: a view of upper-ocean processes in the Bay of Bengal during the southwest monsoon. Oceanography 29(2):134–145 https://doi.org/10.5670/oceanog.2016.46

Mahadevan A, Archer D (2000) Modeling the impact of fronts and mesoscale circulation on the nutrient supply and biogeochemistry of the upper ocean. J Geophys Res 105(C1):1209–1226. https://doi.org/10.1029/1999JC900216

Mahadevan A (2006) Modeling vertical motion at ocean fronts: are nonhydrostatic effects relevant at submesoscales? Ocean Modell 14:222–240

Mahadevan A, Tandon A (2006) An analysis of mechanisms for submesoscale vertical motion at ocean fronts. Ocean Modell. 14(3-4):241–256. https://doi.org/10.1016/j.ocemod.2006.05.006

Mahadevan A, Paluszkiewicz T, Ravichandran M, Sengupta D, Tandon A (2016) Introduction to the special issue on the Bay of Bengal: from monsoons to mixing. Oceanography 29(2):14–17 https://doi.org/10.5670/oceanog.2016.34

Martin PJ (2000) Description of the Navy Coastal Ocean model version 1.0. NRL report no. NRL/FR/7322/00/9962, 45pp. [Available from NRL, Code7322, Bldg. 1009, Stennis Space Center, MS 39529-5004, USA]

Mellor GL (1991) An equation of state for numerical models of oceans and estuaries. J Atmos Ocean Technol 8(4):609–611. https://doi.org/10.1175/1520-0426(1991)008<0609:AEOSFN>2.0.CO;2

Mellor GL, Yamada T (1982) Development of a turbulence closure model for geophysical fluid problems. Rev Geophys Space Phys 20(4):851–875. https://doi.org/10.1029/RG020i004p00851

Metzger EJ, Smedstad OM, Thoppil PG, Hurlburt HE, Cummings JA, Wallcraft AJ, Zamudio L, Franklin DS, Posey PG, Phelps MW, Hogan PJ, Bub FL, DeHaan CJ (2014) US Navy operational global ocean and Arctic ice prediction systems. Oceanography 27(3):32–43 https://doi.org/10.5670/oceanog.2014.66

Rogers WE, Babanin AV, Wang DW (2012) Observation-consistent input and whitecapping-dissipation in a model for wind-generated surface waves: description and simple calculations. J Atmos Ocean Tech 29(1):329–1346

Sarkar S, Pham HT, Ramachandran S, Nash JD, Tandon A, Buckley J, Lotliker AA, Omand MM (2016) The interplay between submesoscale instabilities and turbulence in the surface layer of the Bay of Bengal. Oceanography 29(2):146–157 https://doi.org/10.5670/oceanog.2016.47

Schott FA, McCreary JP (2001) The monsoon circulation of the Indian ocean. Prog Oceanogr 51(1):1–123. https://doi.org/10.1016/S0079-6611(01)00083-0

Schott FA, Xie SP, McCreary JP (2009) Indian Ocean circulation and climate variability. Rev Geophys 47(1):RG1002, https://doi.org/10.1029/2007RG000245

Sengupta D, Bharath Raj GN, Shenoi SSC (2006) Surface freshwater from Bay of Bengal runoff and Indonesian throughflow to the tropical Indian Ocean. Geophys Res Lett 33(22):L22609, https://doi.org/10.1029/2006GL027573

Shetye SR, Gouveia AD, Shenoi SSC, Sundar D, Michael GS, Nampoothiri G (1993) The western boundary current of the seasonal subtropical gyre in the Bay of Bengal. J Geophys Res 98(C1):945–954. https://doi.org/10.1029/92JC02070

Shinoda T, Jensen TG, Flatau M, Chen S (2013) Surface wind and upper ocean variability associated with the Madden-Julian oscillation simulated by the Coupled Ocean-Atmosphere Mesoscale Prediction System (COAMPS). Mon Wea Rev 141:2290–2307

Shulman I, Penta B, Richman J, Jacobs G, Anderson S, Sakalaukus P (2015) Impact of submesoscale processes on dynamics of phytoplankton filaments. J Geophys Res Oceans 120(3):2050–2062. https://doi.org/10.1002/2014JC010326

Smyth WD, Hebert D, Moum JN (1996a) Local ocean response to a multiphase westerly windburst. Part 1: the dynamic response. J Geophys Res 101(C10):22 495–22 512

Smyth WD, Hebert D, Moum JN (1996b) Local ocean response to a multiphase westerly windburst. Part 2: thermal and freshwater responses. J Geophys Res 101(C10):22 513–22 533

Thomas L, Tandon A, Mahadevan A (2008) Submesoscale processes and dynamics. In: Hecht M, Hasumi H (eds) Ocean modeling in an eddying regime, Geophys. Monogr. Ser, vol 177. AGU, Washington, D. C, pp 17–38. https://doi.org/10.1029/177GM04

Wijesekera HW, Gregg MC (1996) Surface layer response to weak winds, westerly bursts, and rain squalls in the western Pacific Warm Pool. J Geophys Res 101(C1):977–997. https://doi.org/10.1029/95JC02553

Wijesekera HW, Paulson CA, Huyer A (1999) The effect of rainfall on the surface layer during a westerly wind burst in the western equatorial Pacific. J Phys Oceanogr 29(4):612–632. https://doi.org/10.1175/1520-0485(1999)029<0612:TEOROT>2.0.CO;2

Wijesekera HW, Paulson CA, Skyllingstad ED (2003) Modeling the evolution of a fresh sea surface anomaly produced by tropical rainfall. J Geophys Res 108(C11):3338. https://doi.org/10.1029/2002JC001408

Wijesekera HW, Jensen TG, Jarosz E, Teague WJ, Metzger EJ, Wang DW, Jinadasa SUP, Arulananthan K, Centurioni LR, Fernando HJ (2015) Southern Bay of Bengal currents and salinity intrusions during the northeast monsoon. J Geophys Res 120(10):6897–6913. https://doi.org/10.1002/2015JC010744